Modelling of hydrogen diffusion in a steel containing micro-porosity. Application to the permeation experiment

Ahmed Yaktiti, Alixe Dreano, R. Gass, T. Yvert, J.F. Carton, Frédéric Christien

Modelling of hydrogen diffusion in a steel containing micro-porosity. Application to the permeation experiment.

A. Yaktiti[1,2], A. Dreano[1], R. Gass[1], T. Yvert[1], J.F. Carton[2], F. Christien[1,]*

[1] Mines Saint-Etienne, Univ Lyon, CNRS, UMR 5307 LGF, Centre SMS, F-42023, Saint-Etienne, France

[2] SafeMetal, 1 Boulevard de la Boissonnette, 42110 Feurs, France

** corresponding author: frederic.christien@emse.fr, +33 7 71 44 04 14*

Abstract

Two numerical models based on non-equilibrium and local equilibrium approaches respectively were developed to simulate hydrogen transport in porous metals, taking account of gaseous hydrogen trapping inside the micro-porosities. They were applied to the case of hydrogen permeation in a cast steel at room temperature. Numerical simulations revealed that the two models are equivalent under certain conditions. A parametric analysis was performed to explore the effect of external hydrogen fugacity, hydrogen solubility and porosity fraction on the hydrogen diffusion behavior. A comparison between experimental permeation data and the numerical results showed reasonable agreement considering no input parameter was adjusted.

Keywords

Hydrogen diffusion and trapping, void, micro-porosity, modelling, FEM, permeation

1. Introduction

Hydrogen embrittlement represents a critical problem for many steels and it can lead to loss of mechanical properties and failure in some cases [1–7]. Due to its small size, hydrogen atom can easily diffuse inside steels. However its diffusivity can be highly affected by microstructural defects known as “traps” such as voids, dislocations, grain boundaries, precipitates and interfaces [8,9]. Therefore, understanding hydrogen diffusion and trapping is a first step in the process of making steel more resistant to hydrogen embrittlement.

Micro-porosity is usually present in near-net shape metallic parts obtained from solidification, as in casting or additive-manufacturing. This micro-porosity is due to volume shrinkage, as well as gas evolution during solidification [10,11]. In cast steels, depending on the process conditions, the volume fraction of porosities is usually of the order of some 10^{-3}, with a porosity size in the micrometer range (see for example the porosity characterization proposed in [12]). Hydrogen is often present as an impurity in as-solidified metal parts. Because of the possible decomposition of water at the liquid metal surface, the presence of humidity in the environment, especially in industrial situations, can result in hydrogen uptake by the liquid metal [13]. In the particular case of cast steels, after cooling, hydrogen can be trapped in micro-porosities as gaseous hydrogen, which can assist the formation of “fisheyes”, a typical hydrogen-related defect [14]. Understanding the hydrogen diffusion and trapping in a steel containing micro-porosities is then of theoretical and practical interest.

In a previous paper [12], experimental data showed that micro-porosity acts as a reversible trap for hydrogen and as a result, it reduces hydrogen diffusivity. This result was obtained based on the comparison between the electrochemical permeation results of forged (non-porous) and cast (porous) specimens obtained from the same low-alloy steel. In addition, it was shown that the majority of hydrogen present in the material was trapped in the porosity. In the present study, the aim is to develop a numerical model, which takes into consideration the role of the porosity in the hydrogen diffusion and trapping processes.

Over the last decades, there has been an extensive effort to develop numerical models that are able to describe hydrogen diffusion and trapping. McNabb and Foster developed a general mathematical model that took into consideration the trapping effect in the hydrogen diffusion process [15,16]. Oriani reformulated their work and provided simpler equations that

are based on the assumption of local equilibrium between lattice and trapped hydrogen [17]. He has shown that the hydrogen apparent diffusion coefficient depends on the trap sites density and the trapping energy. Since then, many works [18–26] have proposed different approaches in order to simulate the hydrogen diffusion process with the presence of traps. All those studies focus on crystal defects only (dislocations, grain boundaries, etc.) and are based on the "effective medium" approach, where the traps are only characterized by a trap density (number of trapping sites per unit volume) and a trap energy. In this "effective medium" approach, the space distribution of traps is ignored and possible lattice hydrogen concentration gradients between traps are neglected (in other terms, the lattice hydrogen concentration is assumed locally homogeneous). These assumptions seem justified if the distance between traps is very small with respect to the specimen size.

In the present work, the focus was set on one specific type of trap, which is the micro-porosity. This porosity can store molecular hydrogen which can lead to hydrogen embrittlement as explained by the hydrogen pressure theory proposed by Zappfe [27]. It assumes that atomic hydrogen H diffuses through the material and recombines as molecular hydrogen H_2 inside the cavities. As a result, the internal pressure rises as atomic hydrogen diffuses until reaching equilibrium between the lattice hydrogen and the hydrogen pressure within the cavity. The distance between micro-pores in a cast steel can be as high as several hundreds of micrometers as shown in [12]. It can be questioned whether the "effective medium" approach is still valid here as such inter-trap distances are not necessarily much smaller than a typical permeation membrane thickness.

Models have been proposed in literature to determine the apparent diffusion coefficient of hydrogen in metals containing porosities [28–30]. With the assumption of a constant equilibrium between the molecular hydrogen trapped in the void and the surrounding hydrogen in the bulk, Chew [28] obtained, in the perfect gas approximation:

$$D_{app} = \frac{D_L}{\left(1 + \frac{2X_P}{RTK_H}\sqrt{P}\right)} \quad (1)$$

with D_{app} the apparent hydrogen diffusion coefficient, D_L the lattice hydrogen diffusion coefficient, X_P the volume fraction of porosity, R the universal gas constant, T the temperature, K_H the hydrogen solubility (Sieverts' constant) and P the local hydrogen

pressure in the voids. Eq. (1) shows how the porosity fraction and the solubility are expected to affect hydrogen diffusion. It is to be noted that the factor of 2 in Eq. (1) should be replaced by a factor of 4, as there is a confusion in the original paper by Chew between the number of moles of molecular hydrogen and that of atomic hydrogen.

More recently, numerical models based on “effective medium” approaches were developed to simulate hydrogen diffusion and trapping in metals containing porosities [31–34]. Note that in those studies, the volume fraction and size of porosities were time-dependent because of embrittling effects of hydrogen itself (blister formation [32,33]) or because of the plastic deformation imposed ([31,33]). Trapping in the porosities was addressed either using a local equilibrium approach (Sieverts’ law) [31,33] or a rate equation of hydrogen recombination/dissociation on the internal porosity surface [32]. It is to be noted that in those studies, hydrogen concentration is assumed homogeneous at the local scale, i.e. the existence of possible hydrogen concentration gradients in the vicinity of the porosities was ignored. In contrast, Zibrov et al. [35] introduced the quasi-stationary approximation to address the existence of a concentration gradient around the porosities. They applied their model to the case a periodic array of nanometric cavities in tungsten to simulate thermodesorption experiments.

Some modelling at a more local scale was also conducted in previous studies [36–39]. However, these studies were limited to the case of a unique cavity embedded in a bulk of metal. In the their evaluation of trapping, Zibrov et al. [39] included both gaseous hydrogen and hydrogen adsorbed on the internal surfaces, the latter being justified by the nanometric size of the cavities. The interface condition was addressed by rate equations involving the three different types of hydrogen in the system (dissolved, adsorbed and gaseous). On the other hand, Sezguin et al. [36,37] have developed an original equation of state for gaseous hydrogen, able to cover a very wide range of pressure and temperature. These authors also pointed out the difficulty in ensuring mass balance when a concentration (i.e. Sieverts’ law) is imposed at the bulk-cavity interface.

In the present study, two different numerical models are proposed in order to study hydrogen diffusion and trapping behavior in steel samples containing porosities. The first model is a 3D finite element model (FEM), where one or several porosities can be introduced. Each porosity is defined by its 3D coordinates and its geometry (only the spherical geometry was considered in this work). The model is based on a non-equilibrium hypothesis, i.e. a

hydrogen flux, at the bulk-porosity interfaces, newly developed for this work in the frame of non-equilibrium thermodynamics. This flux condition at the interface permits to ensure mass balance without any additional computation tricks. In addition, the 3D FEM model developed allows the local description of hydrogen concentration around the porosities, without the quasi-stationary approximation [35]. The second model is a 1D effective medium model based on a local equilibrium hypothesis at the bulk-porosity interfaces. This second model, which is far less computationally expensive, was developed for comparison purpose with the first one. It is to be noted that the mechanical effect of hydrogen pressure inside the porosity was not discussed in this study; the focus was only set on the diffusion and the trapping of hydrogen. In addition, the porosity fraction is considered constant, i.e. no void growth or shrinkage is considered here. The models developed were applied to the case of the well-known permeation experiment. Hydrogen permeation in a low-alloy cast steel (G20MN5) was simulated. The results are compared to permeation experiments from a previous study [12].

2. Numerical models

2.1. Theoretical background

2.1.1. Equation of state (EOS) of gaseous hydrogen

A recent EOS, developed by Sezgin [37], was used in this work (Eq.(2)). This EOS presents the advantage of covering a wide range of pressure and temperature. It is based on the Abel-Noble model and real datasets from the National Institute of Standards and Technology (NIST). It is valid for temperatures above 200 K and pressures as high as 2000 MPa.

$$Pv = RT + Pb^0 - P^2\beta \quad (2)$$

where P is the pressure, v is the molar volume, R is the universal gas constant, T is the temperature, b^0 and β are constants ($b^0 = 1.4598 \times 10^{-5}\, m^3.mol^{-1}$ and $\beta = 1.955 \times 10^{-15}\, m^3.mol^{-1}.Pa^{-1}$).

2.1.2. Hydrogen fugacity

The fugacity of a chemical element (usually noted f) is a thermodynamic function that represents its tendency to escape from a given phase to another [40,41]. The relationship

between the chemical potential of hydrogen μ and hydrogen fugacity f at a constant temperature is:

$$\mu = \mu^0 + RT\, ln\left(\frac{f}{f^0}\right) \quad (3)$$

where μ^0 is the chemical potential of hydrogen at the reference pressure (generally 1 atm) and f^0 is hydrogen fugacity at the reference pressure.

By using and combining thermodynamic relationships, San Marchi *et al.* provided an expression (Eq.(4)) that relates hydrogen fugacity to the pressure [42].

$$ln\left(\frac{f}{P}\right) = \int_0^P \left(\frac{v}{RT} - \frac{1}{P}\right) dP \quad (4)$$

2.1.3. Sieverts' law

The Sieverts' law describes the equilibrium for the dissolution of diatomic gases in metals [43–45]. For hydrogen, the expression is given by Eq.(5) [46]:

$$C_H = K_H\sqrt{f} \quad (5)$$

where C_H represents the concentration of atomic hydrogen dissolved in the material, K_H is the Sieverts' constant (hydrogen solubility) and f is hydrogen fugacity. In this study, we refer to K_H as "Sieverts' constant" or "hydrogen solubility" indifferently.

Sieverts' law can be demonstrated by expressing equilibrium between the respective chemical potentials of hydrogen in the solid phase (H_{Solid}) and the gaseous phase (H_2). Eq.(6) represents the chemical reaction of the dissociation of H_2 into hydrogen atoms.

$$H_2 \leftrightarrow 2H_{Solid} \quad (6)$$

The chemical potential of atomic hydrogen in the solid phase can be expressed as follows:

$$\mu_H^{Solid} = \mu_H^0 + RT\, ln\left(\frac{C}{C^0}\right) \quad (7)$$

where μ_H^0 is the standard chemical potential, C is the H concentration and C^0 is the H concentration at the standard state. In the same way, it is possible to define the chemical potential of molecular hydrogen:

$$\mu_{H_2} = \mu_{H_2}^0 + RT\ ln\left(\frac{f}{f^0}\right) \tag{8}$$

where $\mu_{H_2}^0$ is the standard chemical potential of molecular hydrogen, f represents the hydrogen fugacity and f^0 is the hydrogen fugacity at the standard state. The chemical potential of the atomic hydrogen in the gaseous phase is equal to the half of the chemical potential of the molecular hydrogen:

$$\mu_H^{gas} = \frac{1}{2}\mu_{H_2} \tag{9}$$

At equilibrium, the chemical potentials of hydrogen in the solid and in the gas are equal:

$$\mu_H^0 + RT\ ln\left(\frac{C}{C^0}\right) = \frac{1}{2}\mu_{H_2}^0 + RT\ ln\sqrt{\frac{f}{f^0}} \tag{10}$$

Thus, the equilibrium hydrogen concentration in the solid phase can be expressed as:

$$C = \frac{C^0}{\sqrt{f^0}} \times exp\left(\frac{\frac{1}{2}\mu_{H_2}^0 - \mu_H^0}{RT}\right) \times \sqrt{f} \tag{11}$$

which is the same expression as the Sieverts' law (Eq.(5)), with $K_H = \frac{C^0}{\sqrt{f^0}} \times exp\left(\frac{\frac{1}{2}\mu_{H_2}^0 - \mu_H^0}{RT}\right)$ which is the hydrogen solubility.

2.2. Non-Equilibrium Model

2.2.1. Geometry of the model

In order to simulate hydrogen permeation through a sample containing porosities, the FEM approach was used. The simulations were performed on a 3D geometry as presented in Figure 1 (a) where one of the simulation boxes used in this work is shown. It represents a steel

specimen with one porosity placed in the center. The simulation box has a length of 2 mm. Figure 1 (b) shows a cross-section view.

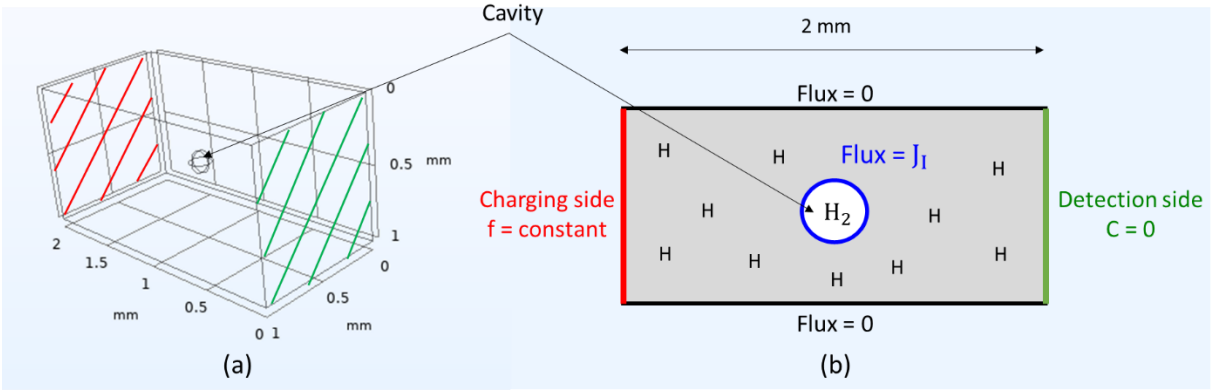

Figure 1 : Simulation box containing one cavity in the center (a) in 3D and (b) cross-section view with the boundary conditions of permeation.

2.2.2. Initial and boundary conditions

A small initial hydrogen concentration was set in the bulk (0.01 mol/m^3) as well as a small initial pressure inside the cavity (0.1 MPa). These non-zero initial conditions avoid numerical problems and it has been checked that they have no influence on the final results.

On the right side of the box, as presented in Figure 1 (b), a zero concentration was imposed, which corresponds to the detection side of the permeation experiment. On the opposite side, a constant fugacity was imposed. This side corresponds to the charging side in the permeation test. Finally, a periodic boundary condition consisting of a zero hydrogen flux was imposed along the lateral sides. Note that because of these periodic boundaries, the elementary box simulated here is equivalent to a 3D network of cavities.

At the bulk-cavity interface, atomic hydrogen can recombine into molecular hydrogen. The key of this model lies in defining the hydrogen flux at the bulk-cavity interface. In our case, it is possible to define this flux using the expression given in Eq.(12) which was developed by Pekar [47]. This is a general expression of the flux (reaction rate) of a chemical reaction between two components A and B based on a non-equilibrium thermodynamics approach:

$$J = k_1 \times exp(-\frac{\mu_A^0}{RT}) \times \left[exp\left(\frac{\mu_A}{RT}\right) - exp\left(\frac{\mu_B}{RT}\right)\right] \qquad (12)$$

where J represents the reaction flux, k_1 is a kinetic factor, μ_A and μ_B are the chemical potential of component A and B, respectively and μ_A^0 is the standard chemical potential of the

component A. In order to use this expression, we must first calculate the chemical potentials of hydrogen in the system. In our case, the chemical potential of atomic hydrogen at the bulk-cavity interface can be expressed as follows:

$$\mu_H^{bulk} = \mu_H^0 + RT\ ln\left(\frac{C_I}{C^0}\right) \tag{13}$$

where μ_H^0 is the standard chemical potential, C_I is the H concentration at the interface and C^0 is the H concentration at the standard state. On the other hand, the chemical potential of atomic hydrogen inside the cavity is:

$$\mu_H^{cavity} = \frac{1}{2}\mu_{H_2}^0 + RT\ ln\sqrt{\frac{f}{f^0}} \tag{14}$$

In order to obtain the hydrogen flux at the bulk-cavity interface, we use Eq.(12) and we substitute μ_A by μ_H^{bulk} (Eq.(13)), and μ_B by μ_H^{cavity} (Eq.(14)). Consequently, the flux at the interface can be expressed as:

$$J_I = k_1 \times exp\left(\frac{\frac{1}{2}\mu_{H_2}^0 - \mu_H^0}{RT}\right) \times \left[exp\left(\frac{\mu_H^0 - \frac{1}{2}\mu_{H_2}^0}{RT}\right) \times \frac{C_I}{C_0} - \sqrt{\frac{f}{f^0}}\right] \tag{15}$$

$$= k_1\left[\frac{C_I}{C_0} - exp\left(\frac{\frac{1}{2}\mu_{H_2}^0 - \mu_H^0}{RT}\right) \times \sqrt{\frac{f}{f^0}}\right]$$

The final expression can be written in the form:

$$J_I = Q \times \left[C_I - K_H \times \sqrt{f}\right] \tag{16}$$

where K_H represents hydrogen solubility as explained earlier with $K_H = \frac{C^0}{\sqrt{f^0}} \times\ exp\left(\frac{\frac{1}{2}\mu_{H_2}^0 - \mu_H^0}{RT}\right)$ and $Q\ =\ k_1/C_0$. In Eq.(16), the term in brackets is a concentration (mol/m^3) and Q, a kinetic factor, has the same unit as a speed (m/s). From the expression above, it can be understood that the orientation of the hydrogen flux at the bulk-cavity interface (inward or outward) depends on the hydrogen concentration at the interface and the hydrogen fugacity inside the cavity. If the hydrogen chemical potential is higher at the interface than inside the cavity (i.e.

$C_I > K_H \times \sqrt{f}$), hydrogen from the bulk will enter the cavity and recombine into molecular hydrogen. In the opposite case ($C_I < K_H \times \sqrt{f}$), hydrogen will quit the cavity and diffuse to the bulk. Finally, at equilibrium ($C_I = K_H \times \sqrt{f}$), the flux is equal to zero. This expression assumes that the porosity act as a reversible trap, i.e. that hydrogen can quit without providing any additional energy from outside the system. This assumption is justified by the experimental data presented in our previous paper [12].

2.2.3. Equations

The module of transport of diluted species [48] provided by Comsol was used to handle the process of hydrogen diffusion in the bulk governed by Fick's law:

$$\frac{\partial C_B}{\partial t} = \nabla.(D\nabla C_B) \tag{17}$$

where C_B is the bulk hydrogen concentration, t is the time and D is the bulk hydrogen diffusion coefficient. The amount of molecular hydrogen inside the cavity (number of moles n) was calculated using Eq.(18). S corresponds to the internal surface of the void and the ½ factor is a stoichiometric coefficient issued from the chemical reaction in Eq.(6).

$$n = \frac{1}{2}\int_S \int_t J_I \, dt \, dS \tag{18}$$

Note that *n* in Eq.(18) is obtained from the interface flux J_I calculated from Eq. (16). The cavity pressure is obtained from Eq.(19), which is one of the two zeros of Eq.(2).

$$P = \frac{(b^0 - v) + \sqrt{(b^0 - v)^2 + 4\beta RT}}{2\beta} \tag{19}$$

where *v* the molar volume is obtained from $v = V_c/n$, with V_c the cavity volume.
Hydrogen fugacity can be obtained by combining Eqs. (2) and (4). At constant temperature, a simple function of pressure is obtained:

$$f = P \times exp\left(\frac{Pb^0 - 0.5 \times \beta \, P^2}{RT}\right) \tag{20}$$

A fully coupled resolution of Eqs. (16) to (20) was conducted to obtain the time variation of the different variables. The main macroscale result extracted is the permeation flux, i.e. the average flux through the entire exit surface of the permeation specimen.

2.2.4. Meshing

The model was meshed by tetrahedral elements generated automatically by Comsol software as presented in Figure 2 (a). A refinement of the meshing was done near the cavities. In order to verify the convergence of the numerical results, the hydrogen permeation flux is plotted as a function of the mesh size in Figure 2 (b). The elements size and the total number of elements are also presented in the same figure, showing no effect of the mesh size on results for the tested condition (one cavity). Furthermore, other simulations were performed by varying the cavity radius (from 4 μm to 100 μm) and the elements size was adapted to ensure the convergence of the results.

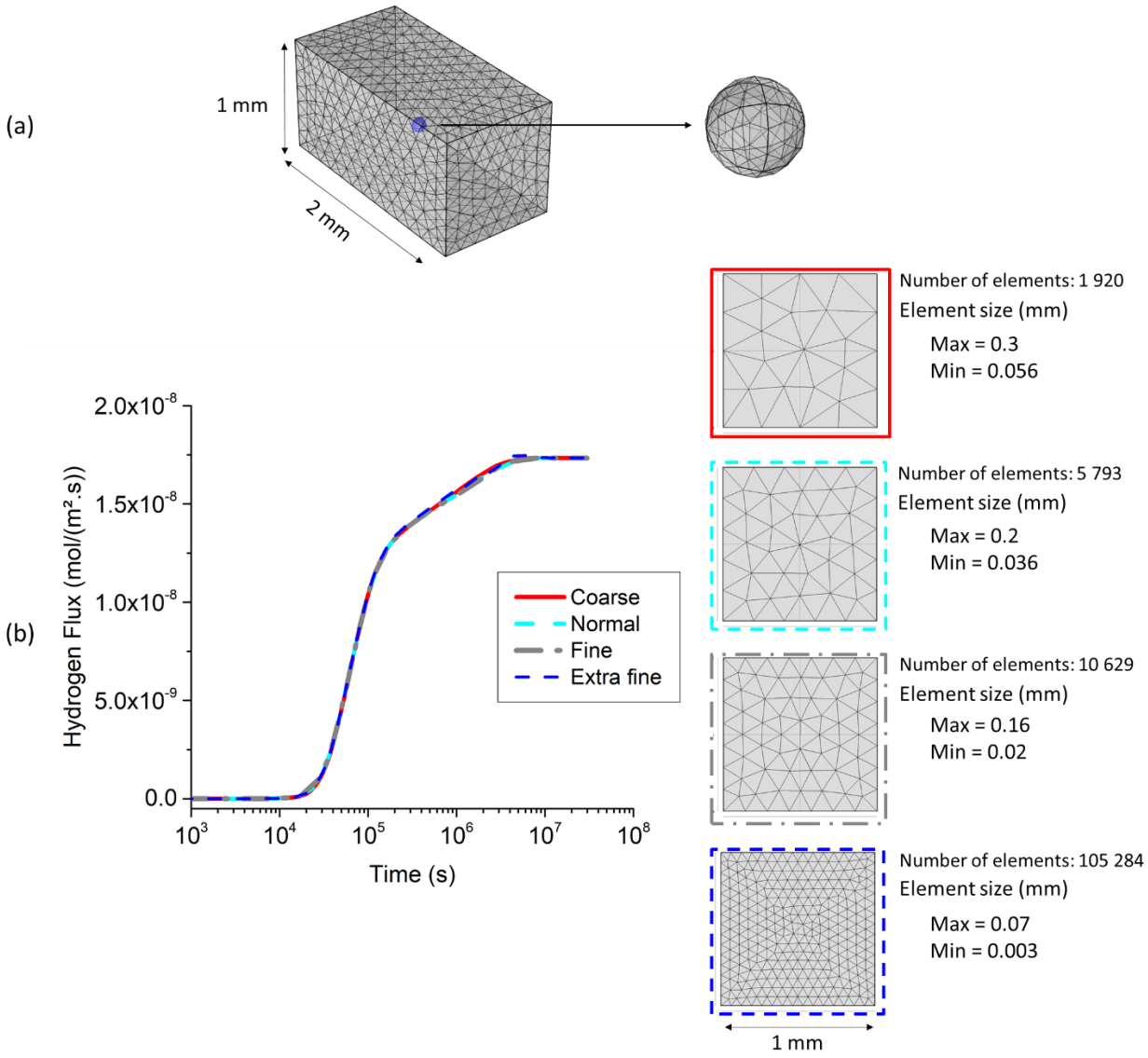

Figure 2: (a) Example of a simulation box used in this study (radius of the cavity: 78 µm); (b) Comparison between the permeation simulated curves obtained using different mesh sizes.

2.3. Local equilibrium Model

A simpler 1D model based on a local equilibrium hypothesis was developed in order to simulate permeation tests in shorter computation times. The main difference between the two models lies in the bulk/porosity interface condition. For the 3D model, a flux is calculated at the interface (Eq.(16)) allowing the description of the reaction $H_2 \leftrightarrow 2H_{Solid}$. The model is then able to describe hydrogen diffusion and trapping inside the porosities even when the equilibrium is not achieved. The 1D model developed in the following only assumes an equilibrium condition at the bulk/porosity interfaces through the Sieverts' law (Eq.(5)). In addition, it is based on an effective medium approach where the space distribution of porosities is not taken into account.

2.3.1. Geometry, boundary and initial conditions

Figure 3 shows a schematic representation of the 1D simulation box with a length of 2 mm. The sample was split along the thickness into k equivalent elements. The number of elements is high enough to ensure the convergence of the calculations ($k = 50$). The porosity fraction in each element is the same and it is equal to the porosity fraction of the sample.

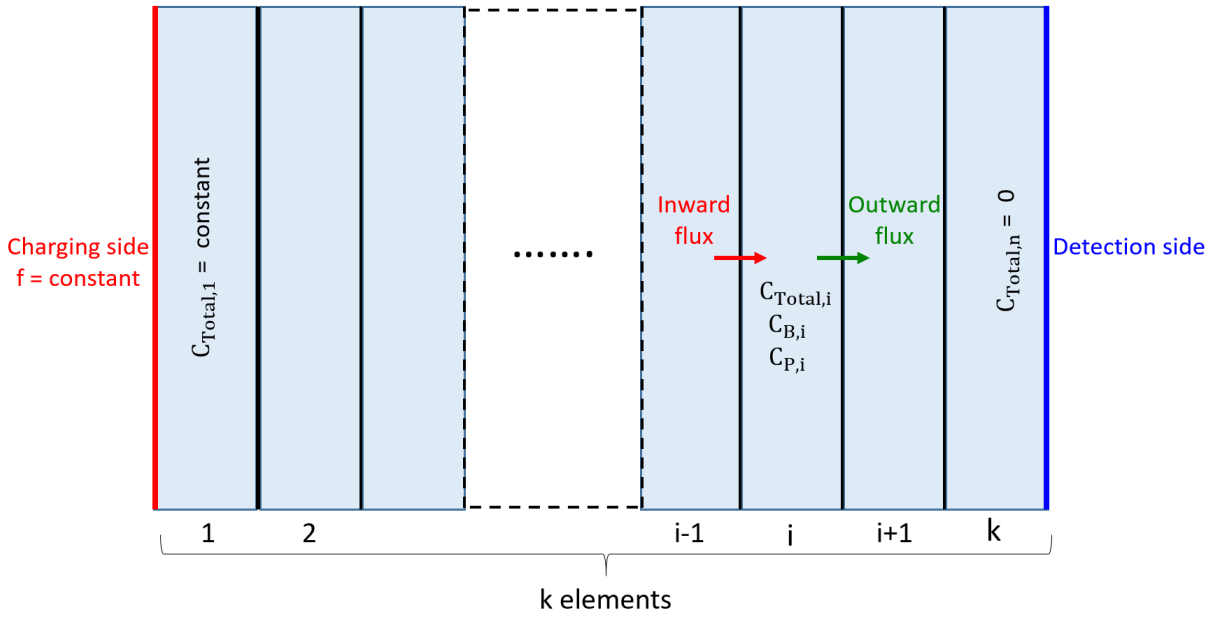

Figure 3 : Schematic representation of the simulation box used in the local equilibrium model.

The boundary conditions are presented in Figure 3. The first element corresponds to the charging side where the fugacity inside the porosity is equal to the fugacity of the charging medium and the bulk concentration is deduced from Sieverts' law (Eq.(5)). The last element represents the detection side where the concentration was set to zero. These boundary conditions were maintained during the whole simulation. In addition, the initial hydrogen concentration was set to zero in elements 2 to $k - 1$.

2.3.2. Equations

In each element, the bulk hydrogen concentration is constantly in equilibrium with the hydrogen fugacity trapped in the cavities as described by Sieverts' law. This equilibrium is instantly established and only bulk hydrogen is able to diffuse from one element to another. The total hydrogen concentration C_{Total} in each element is the sum of bulk hydrogen concentration C_B and hydrogen concentration in the porosity C_P as expressed in Eq.(21).

$$C_{Total} = C_B + C_P \tag{21}$$

Hydrogen diffusion, in each element and at each time step, is calculated using Fick's law:

$$\frac{\partial C_{Total}}{\partial t} = \nabla.(D\nabla C_B) \quad (22)$$

where C_{Total} is the total hydrogen concentration, D is the bulk diffusion coefficient and C_B is the hydrogen bulk concentration. Note that, in the second term of the equation, C_B is used instead of C_{Total}. Equilibrium between bulk and trapped hydrogen is maintained at each time step. For a given C_{Total}, the corresponding C_B can be obtained from a set of equations composed of Eq.(2), (4), (5) and (21). It appeared that numerical solving of that system of equations was very time consuming. In addition, multiple zeros were obtained and the zero selection process was not easy to automate. For these reasons, we have opted for a pre-calculated table of solutions which is composed of C_{Total} and the corresponding C_B and C_P for a given porosity fraction. At equilibrium, for a given C_{Total}, the possible values of C_B and C_P are unique. The values of C_B and C_P corresponding to a given C_{Total} are extracted from the table of solutions using linear interpolation. Finally, it should be mentioned that the extracted permeation flux corresponds to the flux calculated at the interface of the $(k-1)$ element and the (k) element. The model was implemented in a Matlab code using the "ode15s" function.

2.4. Input Parameters

The input parameters used in the numerical simulations are presented in table 1. The value of the fugacity was estimated using the work of Venezuela [49], which gives a relationship between hydrogen fugacity and the electrochemical over-potential for a 3.5NiCrMoV steel charged in a 0.1 M NaOH aqueous solution. In our electrochemical permeation tests, presented in our previous article [12], the over-potential was equal to -1.1V, which corresponds to a fugacity of 60 MPa. Furthermore, the hydrogen diffusion coefficient used in the simulations is the apparent diffusion coefficient of the forged sample (i.e. without porosity) calculated using the time-lag method based on the electrochemical permeation results [12]. The solubility coefficients are also taken from our previous work [12] and from literature as stated in Table 1. Finally, the porosity fractions were obtained by the hydrostatic weighing technique on cast samples in [12].

Table 1 : Input parameters used in the numerical simulations.

Parameter	Values
Solubility, K_H (mol/(m^3 x MPa$^{0.5}$)	[0.025 [36]- 0.711 [12]]
Hydrogen fugacity of the charging medium, f (MPa)	60
Diffusion coefficient, D (m²/s)	7.8×10^{-12}
Membrane thickness (mm)	2
Temperature, T (°C)	20
Porosity volume fraction, X_P (%)	[0.02 - 0.4]
Recombination/dissociation kinetic factor, Q (m/s)	[10^{-9} – 10^{-3}]

3. Results and discussion

3.1. Non-Equilibrium Model

3.1.1. One cavity case - Effect of the kinetic factor Q

The aim of the first simulations was to understand the effect of the kinetic factor Q of Eq.(16) on the permeation behavior. This factor affects directly the flux of hydrogen at the bulk-cavity interface. Physically, it affects the reaction rate of the recombination of atomic hydrogen into molecular hydrogen. A one cavity simulation box was used (as presented in Figure 1) with a porosity fraction of 0.04% (cavity radius of 78 µm) and a solubility coefficient of 0.569 mol/(m^3×MPa$^{0.5}$). The side length of the numerical box is equals to 1 mm. Several simulations with different values of Q are given in Figure 4, showing the permeation curve (Figure 4 (a)) and the pressure evolution (Figure 4 (b)). The results obtained when no porosity is present are also shown. For very low values of Q ($Q \leq 10^{-8}\ m/s$), the permeation curves are the same as in the case without porosity. This is because the flux entering the cavity at any time is negligible compared to the permeation flux, so that the permeation curve is not significantly affected. For $Q \geq 10^{-7}\ m/s$, the permeation curves deviate from the case without porosity from approximately $t \geq 10^5 s$, which corresponds to the time when the cavity pressure starts to rise. In this case, the flux entering the cavity is significant (in the transient regime) and affects the global permeation behavior. It is to be noted that for $Q \geq 10^{-6}\ m/s$, the results converge to a single solution, that does not depend on Q. This means that the hydrogen entry in the cavity is not governed any more by the kinetics of the surface reaction, but rather by the local hydrogen diffusion around the cavity. As shown in the next section, hydrogen concentration gradients exist in the transient state around the cavity, which

limit the flux entering the cavity. In the present work, we have chosen to conduct the simulations in the regime where local hydrogen diffusion is the limiting step. All the simulations presented later were performed with $Q = 10^{-4}\ m/s$.

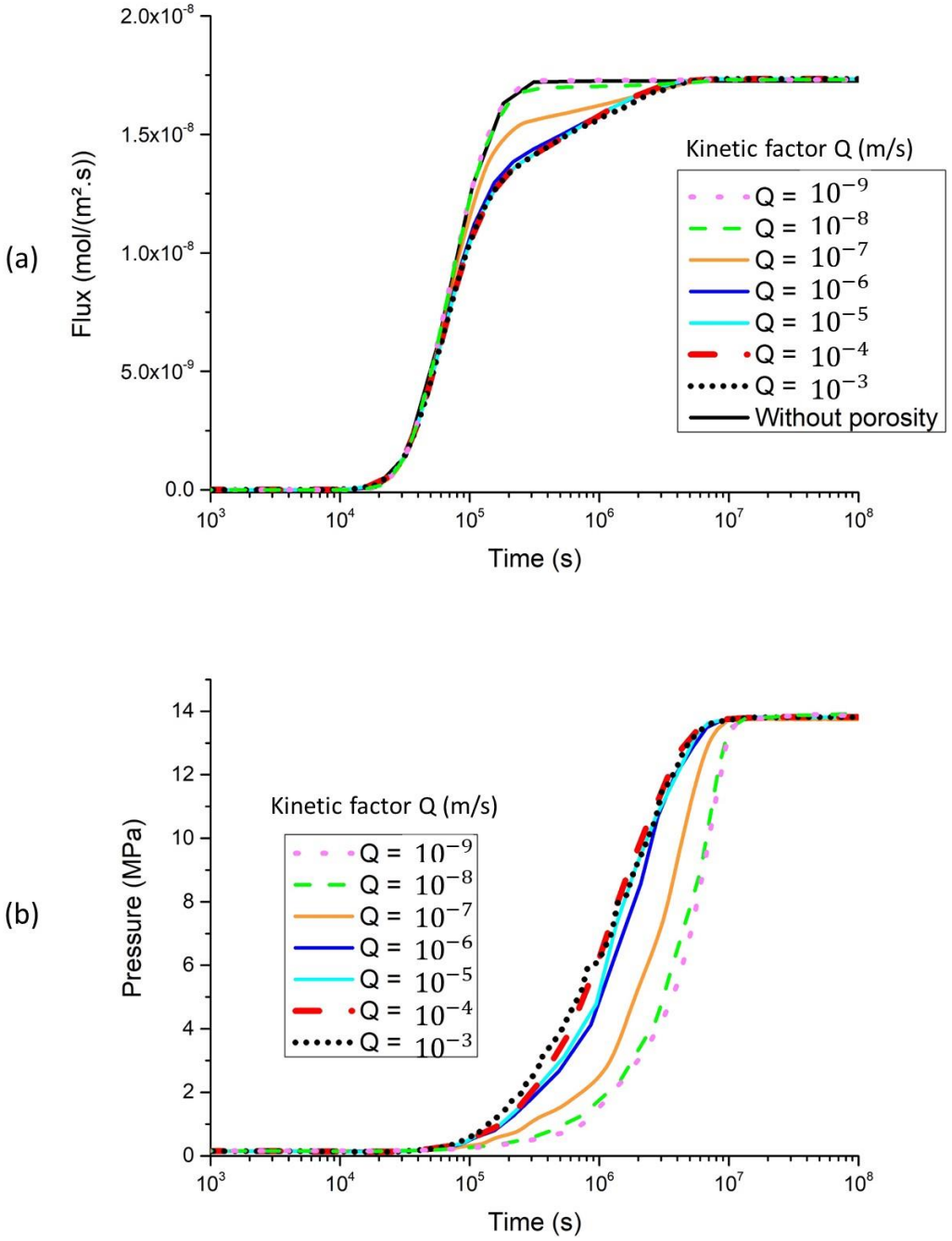

Figure 4 : Influence of the kinetic factor Q on (a) the permeation flux and on (b) the evolution in time of the pressure inside the one cavity model. $K_H = 0.569\ mol/(m^3 \times MPa^{0.5})$; $X_P = 0.04\%$.

3.1.2. One cavity case in the local diffusion-limited case

Figure 5 presents the simulation results of a permeation test for a sample containing one cavity (red curve), with $Q = 10^{-4}\ m/s$ (local diffusion-limited regime). The other input parameters are the same as in the previous section. The permeation flux is presented in Figure 5 (a). The case without porosity is also considered for reference. The time evolutions of the hydrogen concentration and flux at the bulk-cavity interface are shown in Figure 5 (b) and (c) respectively. Note that these values are averaged over the interface. Figure 5 (d) gives the time dependence of the cavity pressure.

In Figure 5 (a), the fluxes of the two simulations start to rise at the same time (≈ 2×10^4 s). This means that, even in the one cavity case, a significant amount of hydrogen is able to travel across the specimen without interacting with the cavity. However, the 1 cavity simulation shows a change in slope at about $6\text{x}10^4$ s and reaches the steady state later. These differences are due to the hydrogen-cavity interaction. The change in slope in Figure 5 (a) corresponds to the moment when the hydrogen uptake in the cavity becomes significant (Figure 5 (c) and (d)). The difference in time needed to reach the permeation steady state between the two simulations of Figure 5 (a) is related to the time needed to equilibrate the pressure in the cavity (Figure 5 (b), (c) and (d)). In the steady state ($t > 5\ 10^6$ s), the hydrogen concentration at the bulk-cavity interface and the cavity pressure are constant and obey the Sieverts' law. This gives a zero net flux entering the cavity (Figure 5 (c)) as expected from Eq. (16).

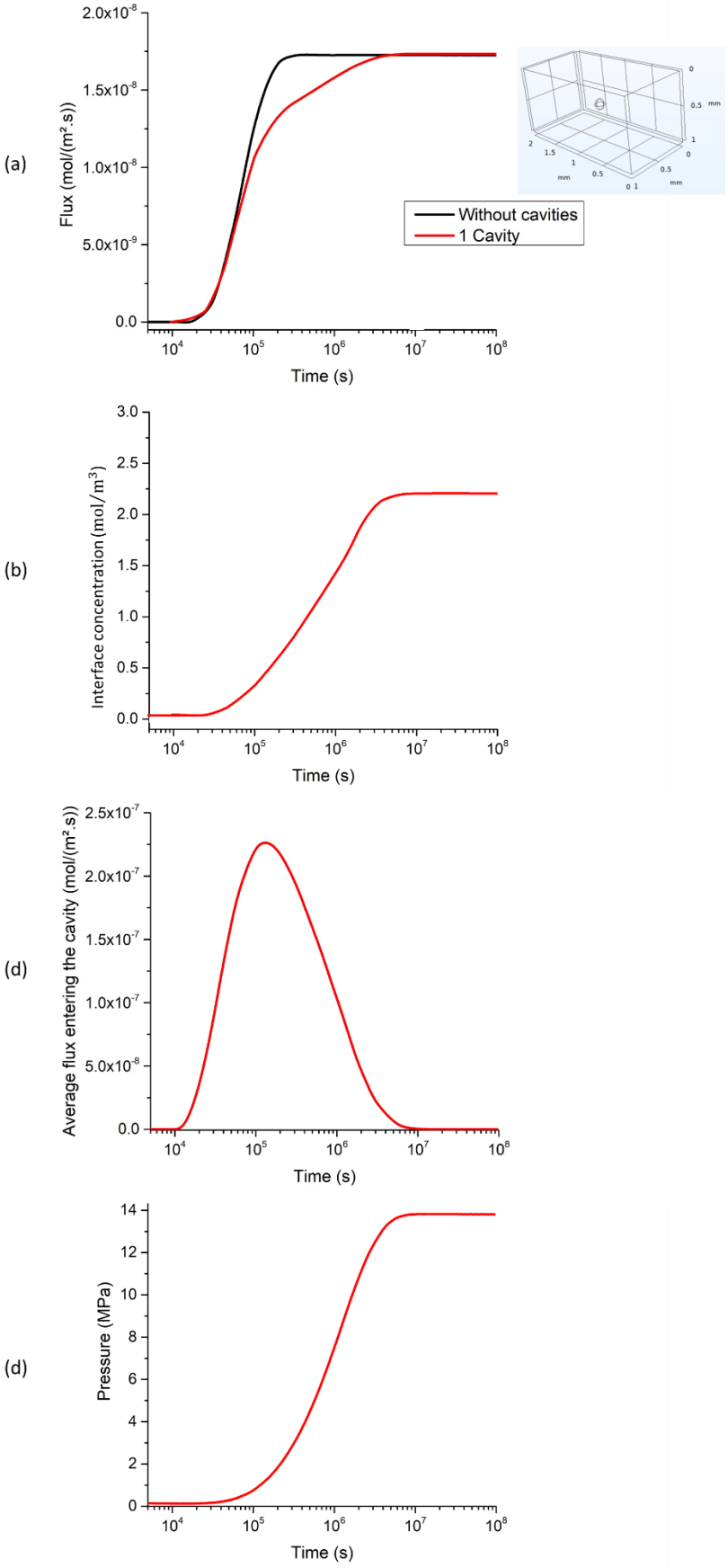

Figure 5: (a) Comparison of the hydrogen permeation flux obtained by numerical simulation for a case without cavity (black curve) and a case with one cavity (red curve); (b) Average hydrogen concentration at the bulk-cavity interface; (c) Average hydrogen flux at the bulk-cavity interface; (d) Pressure inside the cavity. $K_H = 0.569\ mol/(m^3 \times MPa^{0.5})$; $X_P = 0.04\%$; $Q = 10^{-4}\ m/s$.

Figure 6 (a) shows the 1D concentration profiles of bulk hydrogen along a line intersecting the cavity at different times. The discontinuity in the profiles corresponds to the cavity, where the hydrogen bulk concentration is not defined. As soon as hydrogen reaches the cavity (dark blue curve), the concentration starts to rise at the interface. However it is to be noted that for the duration of the transient regime, steep concentration gradients are observed in the vicinity of the cavity, which is expected in a diffusion-limited regime. In the stationary regime (light blue curve), an almost linear profile is obtained throughout the specimen and the hydrogen concentration at the metal-cavity interface is constant. This concentration corresponds to the local equilibrium as described by Sieverts' law (Eq.(5)), which indicates that the chemical potential of the hydrogen at the interface is in equilibrium with the chemical potential of the hydrogen cavity pressure. Figure 6 (b) represents hydrogen concentration 2D maps in a plane intersecting the cavity at different times. The lines plotted on the maps represent the local hydrogen fluxes. In the transient regime ($t > 4.5\ 10^5$ s), local concentration gradients and fluxes towards the cavity are evidenced.

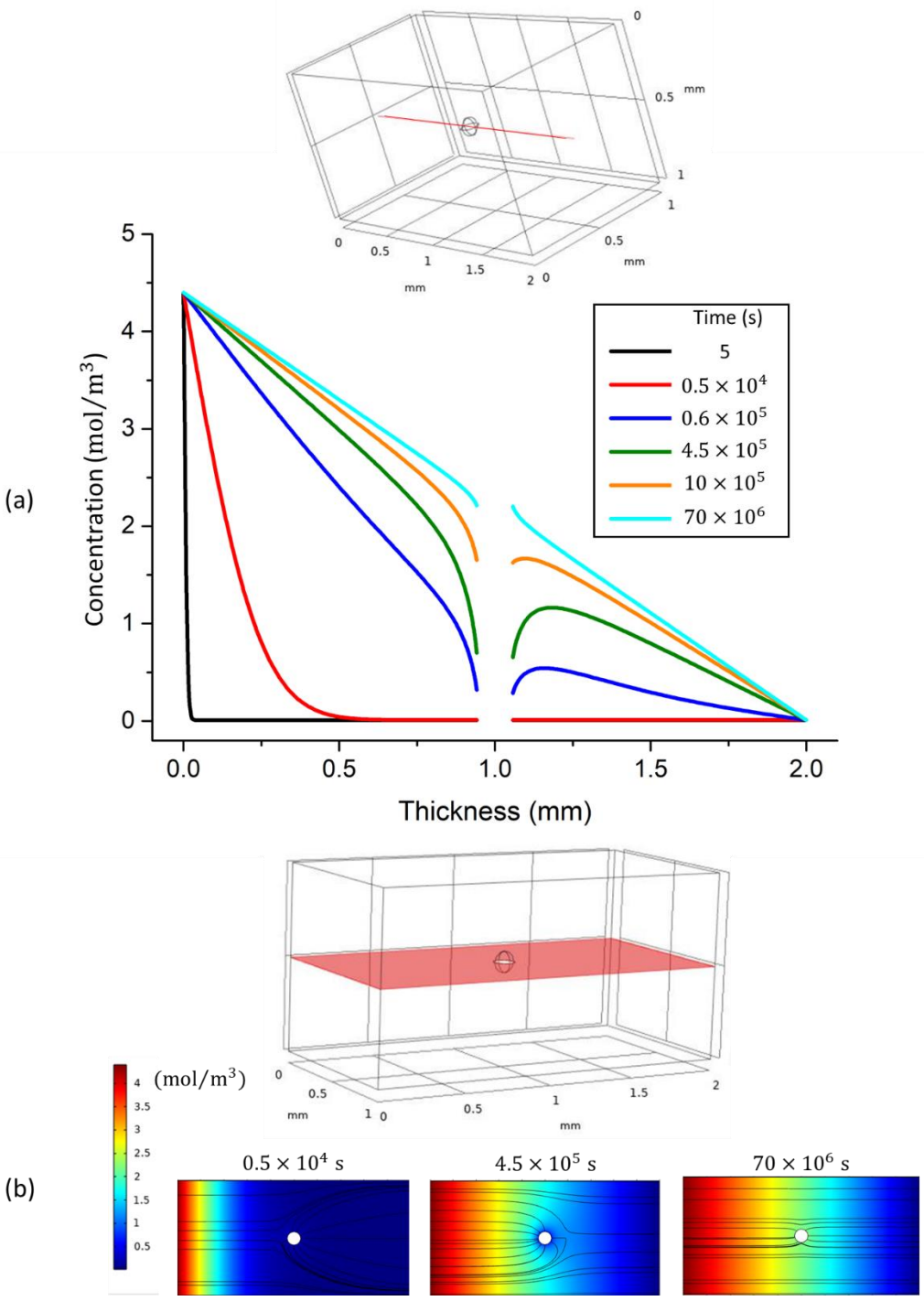

Figure 6: (a) 1D hydrogen concentration profiles at different times along a line intersecting the cavity; (b) 2D hydrogen concentration maps at different times in a plane intersecting the cavity. The lines shown in the maps represent the local hydrogen fluxes. $K_H = 0.569\ mol/(m^3 \times MPa^{0.5})$; $X_P = 0.04\%$; $Q = 10^{-4}\ m/s$.

Figure 7 presents the effect of the hydrogen solubility (Sieverts' constant K_H) on the permeation curve. It is reminded here that hydrogen fugacity at the entry side is kept constant (60 MPa). Figure 7 (a) shows that the stationary flux increases with increasing solubility. This is in agreement with the Sieverts' law (Eq.(5)) predicting that hydrogen concentration at the entry side increases linearly with solubility. It is shown in Figure 7 (b) that the time needed to

reach the permeation steady state is longer for smaller solubility constants. This can be easily understood as it will take more time to reach the steady state cavity pressure when the average bulk hydrogen concentration surrounding it is smaller.

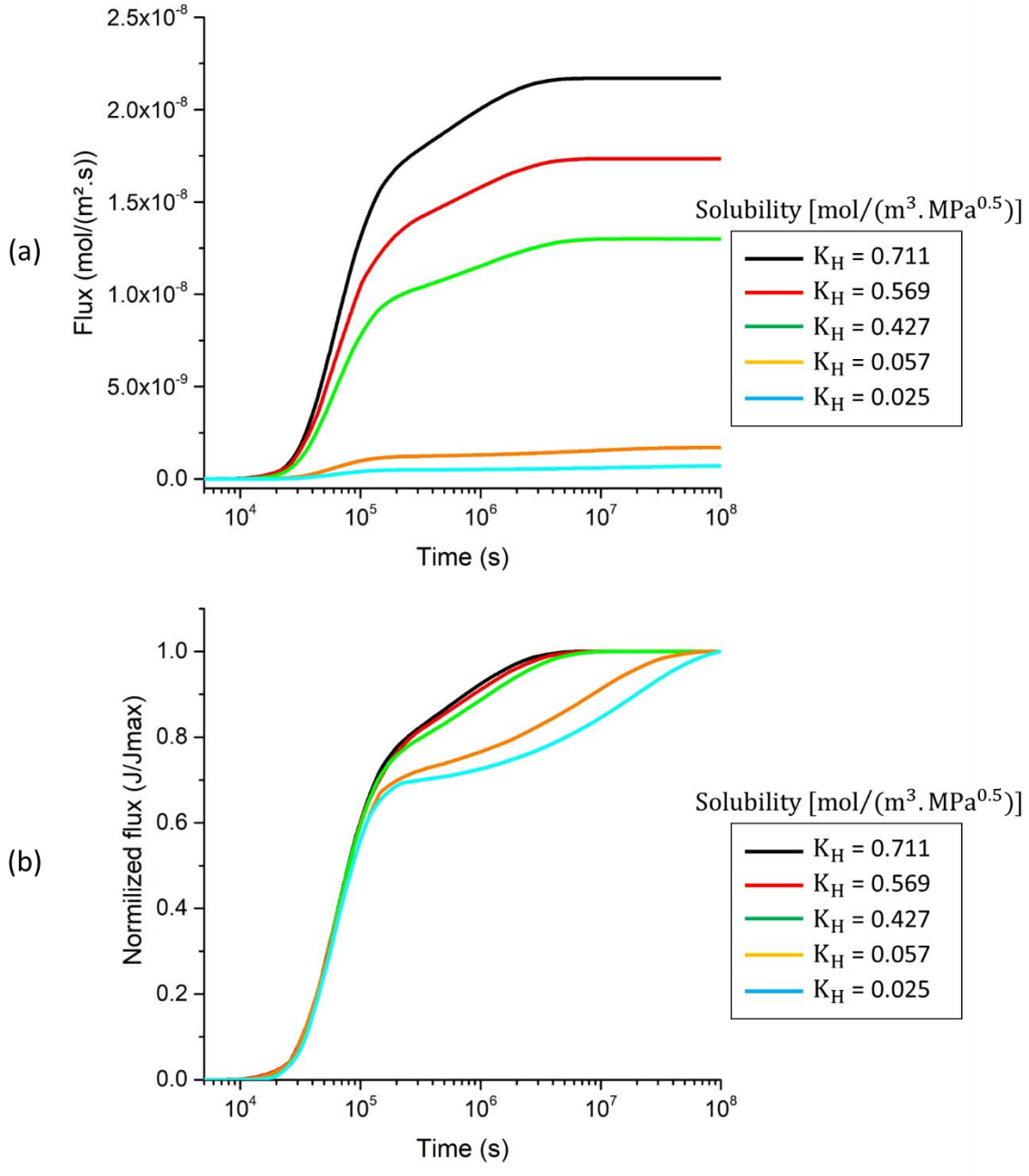

Figure 7 : Influence of the hydrogen solubility K_H on the permeation flux. (a) Non normalized flux; (b) normalized flux. $X_P = 0.04\%$; $Q = 10^{-4}\ m/s$.

3.1.3. Multiple cavity case with periodic network

In this section, the results were obtained from several simulations performed on boxes that have different numbers of cavities. The aim was to highlight the effect of the distribution of cavities on the permeation behavior. It should be noted that the porosity fraction was maintained constant at the same value (0.04%) for all the simulations in order to exclude the effect of the porosity fraction on the results. The same value of Q as in the previous section was used ($Q = 10^{-4}\ m/s$). In order to keep a homothetic network of cavities, the box size, more particularly the side length, had to be modified in each case (the thickness was kept the same, i.e. 2 mm). Table 2 summarizes the geometric parameters and the different characteristics of the simulation boxes used in this work. All the numerical simulations were performed using the same solubility coefficient (0.569 mol/(m^3×$MPa^{0.5}$)). As an example, Figure 8 shows a simulation box containing 5 cavities of the same radius.

Table 2: The characteristics and the geometric parameters of the 3D simulation boxes.

Number of cavities	0	1	2	5	10	20
Inter-cavity distance (mm)	-	-	1	0.4	0.2	0.1
Cavity radius (µm)	-	78	39	16	8	4
Specimen thickness (mm)	2	2	2	2	2	2
Side length (mm)	1	1	0.5	0.2	0.1	0.05
Porosity fraction (%)	0.04	0.04	0.04	0.04	0.04	0.04

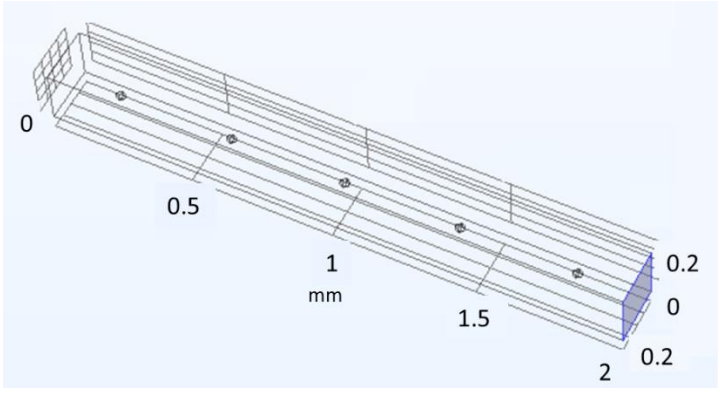

Figure 8**:** Example of a 3D simulation box used in this study for the case with 5 cavities. The network of cavities is kept homothetic.

Figure 9 shows the influence of the number of cavities on the permeation flux. The hydrogen flux for all the simulations starts to rise at 2×10^4 s and then the increase of the flux becomes different from one case to another. The flux of the simulation without cavity increases faster than the others do because hydrogen diffuses without being trapped. By comparing the different curves, it is obvious, until 4×10^5 s approximately, that the slope decreases with increasing the number of cavities. Actually, the increase of number of cavities at constant porosity fraction increases the bulk-cavity interface area. Hence more interface area is available for hydrogen recombination. This increases the amount of hydrogen trapped in a given time increment. Thus, less hydrogen is available to diffuse and reach the detection side, which explains the slower increase in the hydrogen permeation flux. However, it was found that the number of cavities has no more effect on the permeation behavior for simulations with 10 cavities or more. On the other hand, after 4×10^5 s, there is a change in the permeation behavior. The simulation with one cavity reaches the steady state last. This is related to the surface-to-volume ratio of the cavities. In the 1 cavity case, this ratio is minimum, so that the time needed to fill the cavity is maximum and, as a result, the steady state is delayed.

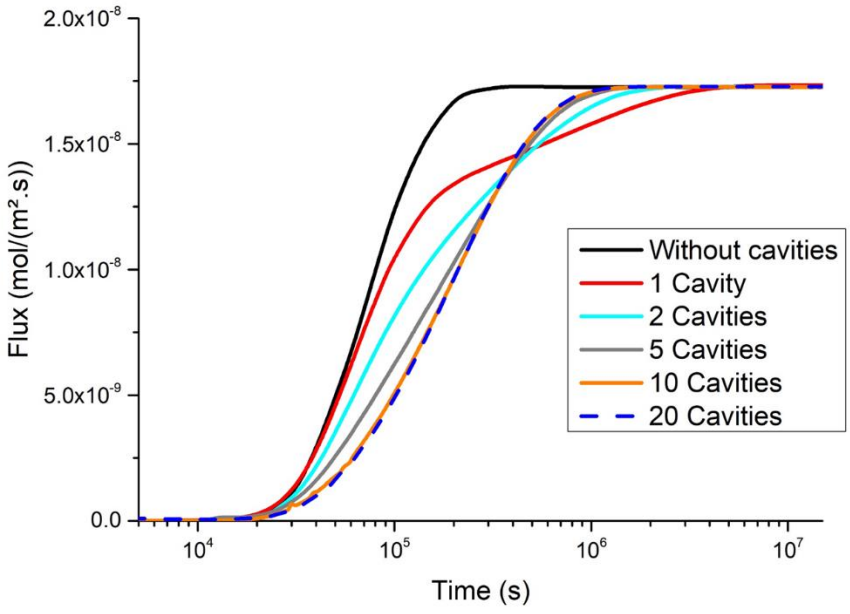

Figure 9: Effect of the number of cavities on the hydrogen permeation flux. $K_H = 0.569\ mol/(m^3 \times MPa^{0.5})$; $X_P = 0.04\%$; $Q = 10^{-4}\ m/s$.

Figure 10 shows the time evolution of the pressure inside the cavities for the simulation with 10 cavities. The pressure stays very low at the beginning and then, when hydrogen atoms reach each cavity, the pressure starts to rise, but at different moment depending on the cavity position. The cavity near the charging side has the highest pressure and the cavity near the detection side has the lowest as it can be expected considering the boundary conditions.

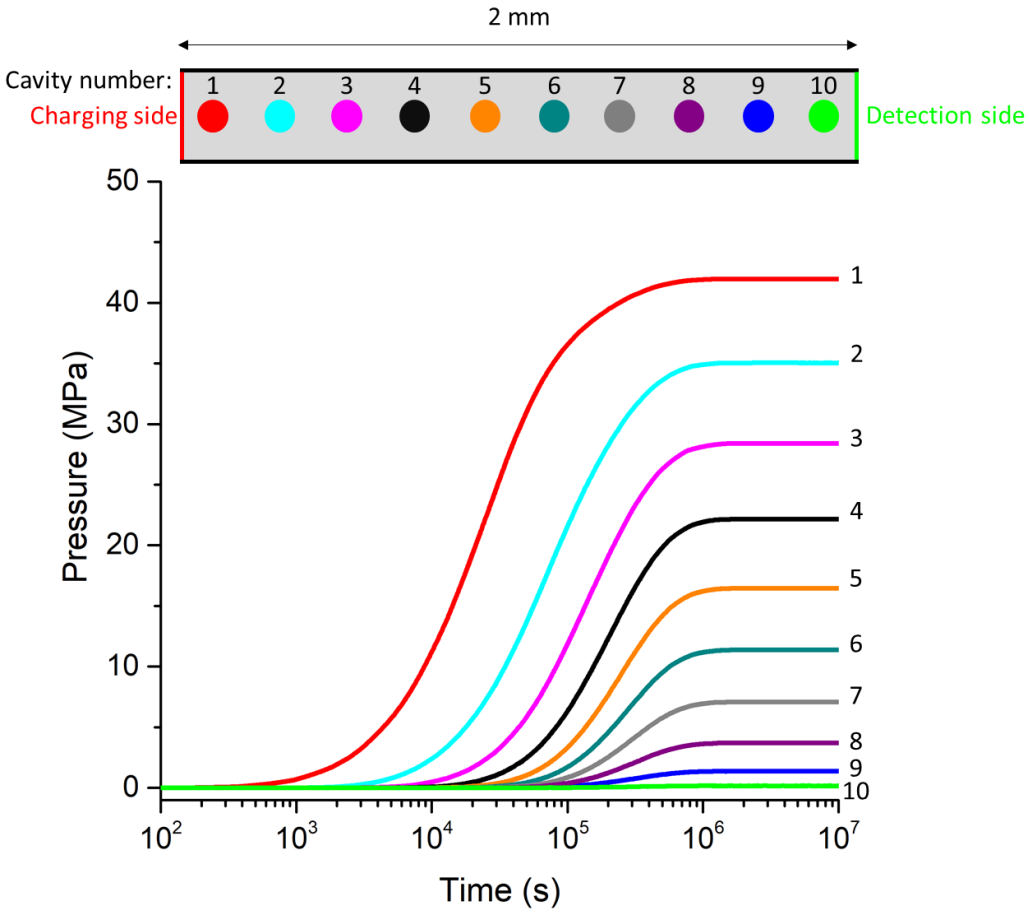

Figure 10: Time evolution of the pressure inside the cavities. $K_H = 0.569\ mol/(m^3 \times MPa^{0.5})$; $X_P = 0.04\%$; $Q = 10^{-4}\ m/s$.

3.1.4. Multiple cavity case with random network

Figure 11 shows the permeation curves (Figure 11 (a)) obtained for simulations boxes containing ten randomly distributed cavities. In case 1, the location of cavities is fully random, whereas in cases 2 and 3, the cavities are located closer to the entry side or to the exit side respectively (Figure 11 (b)). The case without porosity is also shown for comparison. The permeation behavior in the fully random case (case 1) is not significantly different from that obtained with a periodic network of cavities. In case 2, the trapping effect of porosity is slightly

increased with respect to case 1. This is because the amount of hydrogen trapped in the cavities is higher in case 2 (the average cavity pressure is higher as the cavities are located closer to the entry side). The same reasoning can be done for case 3 where the trapping effect is smaller when cavities are located closer to the exit side.

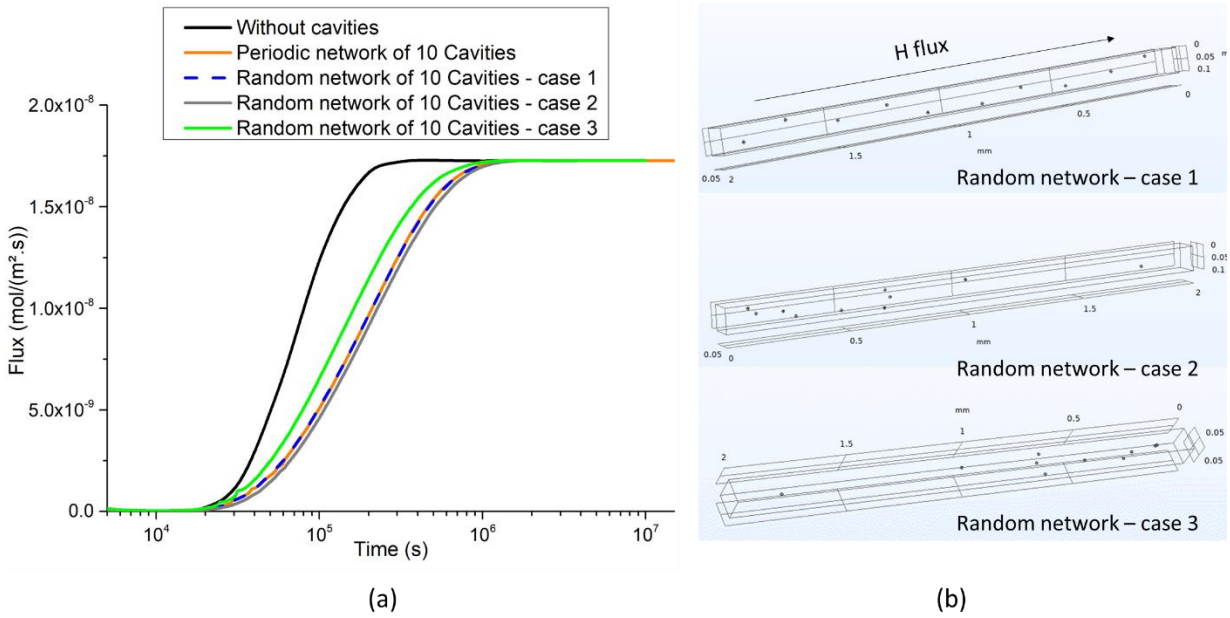

Figure 11: Effect of the cavity space distribution on the hydrogen permeation flux: (a) the permeation curves; (b) distribution of cavities inside the simulation box. $K_H = 0.569\ mol/(m^3 \times MPa^{0.5})$; $X_P = 0.04\%$; $Q = 10^{-4}\ m/s$.

3.2. Local equilibrium model

3.2.1. First results and comparison to the non-equilibrium model

The equilibrium model was run using a constant porosity fraction of 0.04% and a solubility coefficient of 0.569 mol.m^{-3}.MPa$^{-1/2}$. Results are presented in Figure 12 and compared to the non-equilibrium model with 10 cavities.

Figure 12 (a) presents the obtained permeation fluxes as a function of time using the two models. The red dashed curve corresponds to the result of the non-equilibrium model with 10 cavities and the black curve corresponds to the result of the local equilibrium model simulation. Interestingly, the same permeation behavior was found in the two cases. This shows that the two models are equivalents when the non-equilibrium model is used with a sufficiently high number of cavities. For further confirmation of this conclusion, the pressure

profiles across the specimen at steady-state were also compared for the two models (Figure 12 (b)). The same values of pressure are obtained, which confirms the equivalence between the two models when a large number of cavities is used in the non-equilibrium model. This is made possible by the larger bulk-cavity interface area and the smaller cavity volume, which facilitates the establishment of local equilibrium. This equivalence is an important point because the local equilibrium model is easier and simpler to use than the non-equilibrium model. In particular, the calculation time is incomparable. In the following, the local equilibrium model was used to study the influence of the porosity fraction, the solubility coefficient and the fugacity of the charging medium on the permeation behavior.

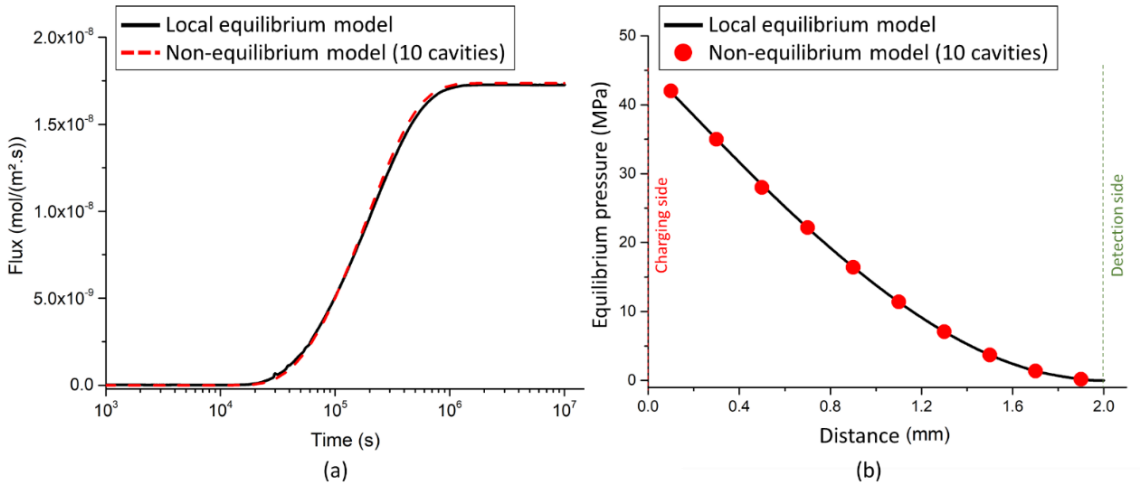

Figure 12: Comparison between the non-equilibrium model and the local equilibrium model: (a) hydrogen permeation flux as a function of time and (b) steady state pressure profile in the cavities across the specimen thickness. $K_H = 0.569\ mol/(m^3 \times MPa^{0.5})$; $X_P = 0.04\%$; $Q = 10^{-4}\ m/s$.

3.2.2. Porosity fraction effect

Figure 13 (a) summarizes the results of various simulations performed with different porosity fractions. The porosity fraction vary from 0% to 0.4%. The solubility coefficient is still fixed to 0.569 mol.m^{-3}.MPa$^{-1/2}$.

In Figure 13 (b), the time needed to reach $J_{max}/2$ is correlated to the porosity fraction. It shows that, under the conditions tested here, the diffusion time increases linearly with increasing the porosity fraction, which is in agreement with the expression of the apparent diffusion coefficient D_{app} presented in Eq. (1).

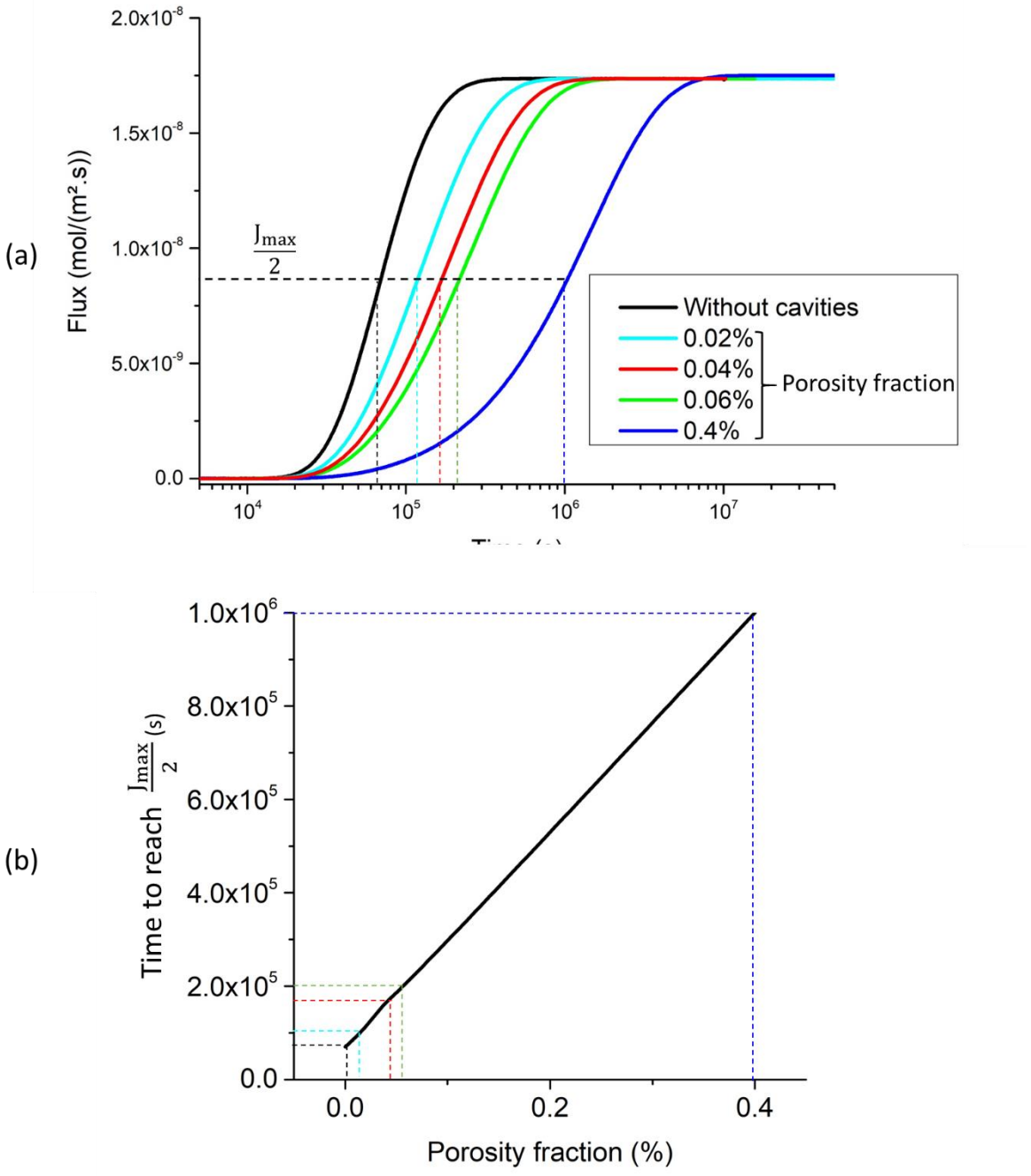

Figure 13: (a) Influence of the porosity fraction on the hydrogen permeation flux; (b) Evolution of the time to reach $J_{max}/2$ as a function of the porosity fraction. $K_H = 0.569\ mol/(m^3 \times MPa^{0.5})$.

3.2.3. Hydrogen solubility effect

Four different calculations have been performed in order to determine the influence of the solubility coefficient on the permeation behavior (Figure 14 (a)) while keeping the other parameters constant. It should be mentioned that the hydrogen concentration on the charging side was different from one case to another. Actually, as mentioned earlier, a constant fugacity of 60 MPa was applied on the charging side, thus the hydrogen

concentration varies when varying the solubility coefficient. As a result, the steady state flux was not the same for all the simulations. In order to make the comparison easier, the normalized flux J/J_{max} is plotted in Figure 14 (b). Results showed that increasing the solubility tends to decrease the permeation time. This is expected as the increase of hydrogen solubility reduces the trapping effect of porosity. Therefore, the hydrogen flux increases faster. In Figure 14 (c), the time to reach $J_{max}/2$ is plotted with respect to the solubility coefficient. It indicates that the permeation time and the solubility coefficient have an inverse relationship, which is in agreement with Eq. (1).

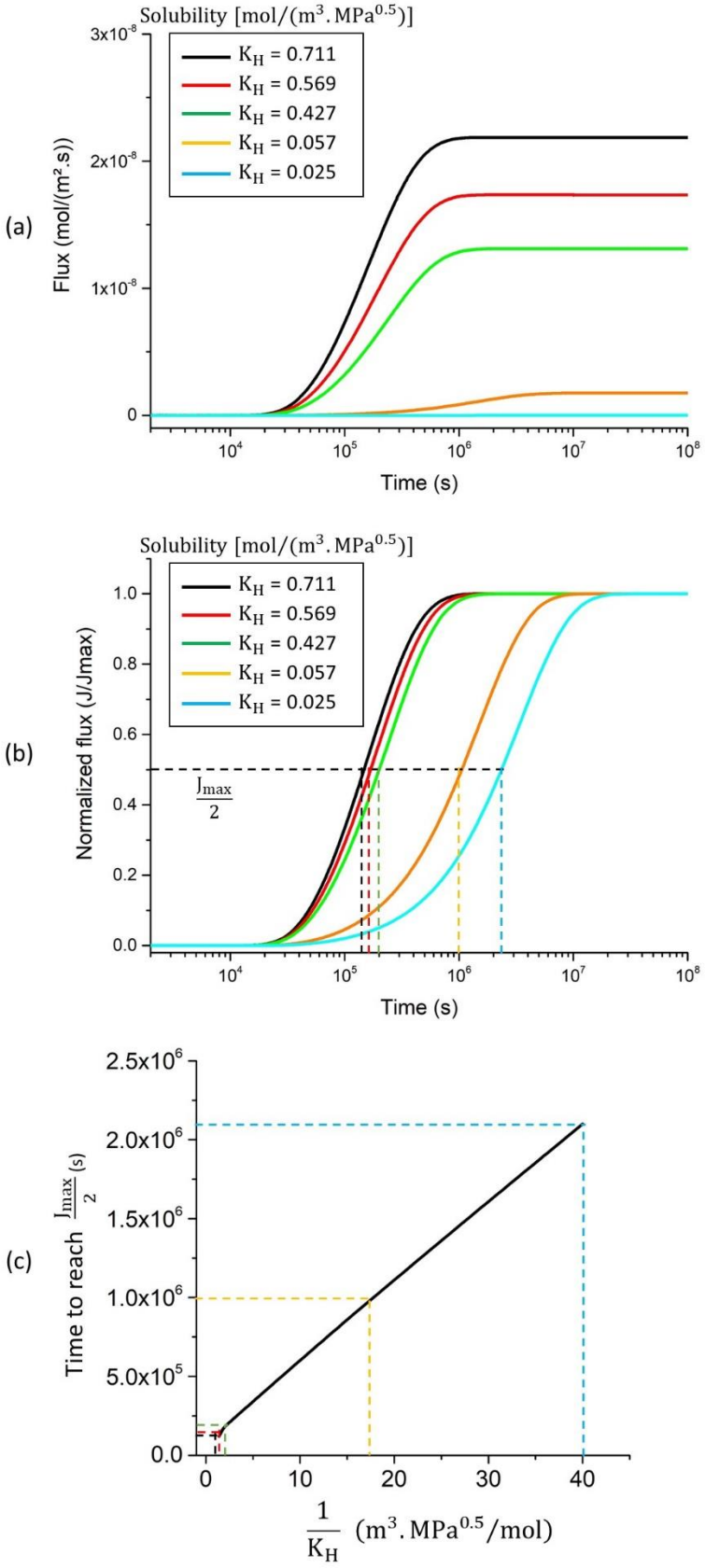

Figure 14: Effect of the solubility coefficient on the hydrogen permeation flux (a) before normalization and (b) after normalization. (c) Evolution of the time needed to reach $J_{max}/2$ as a function of the solubility coefficient. $X_P = 0.04\%$.

3.2.4. Hydrogen fugacity effect

In this section, the influence of hydrogen fugacity of the charging medium, i.e. at the entry side, on the permeation behavior was discussed. For all the simulations, the porosity fraction was equal to 0.04% and the solubility coefficient was equal to 0.569 mol/(m^3×$MPa^{0.5}$). Figure 15 (a) shows the normalized permeation curves for different hydrogen fugacities. As it can be seen, the hydrogen flux rises faster and reaches the steady state earlier in the case of low fugacities compared to high fugacities. In order to better visualize this effect, the relationship between the time needed to reach J_{max} / 2 and hydrogen fugacity is presented in Figure 15 (b). The relationship indicates that the permeation time increases approximately as the square root of hydrogen fugacity. Once again, this conclusion is in concordance with the expression given in Eq. (1).

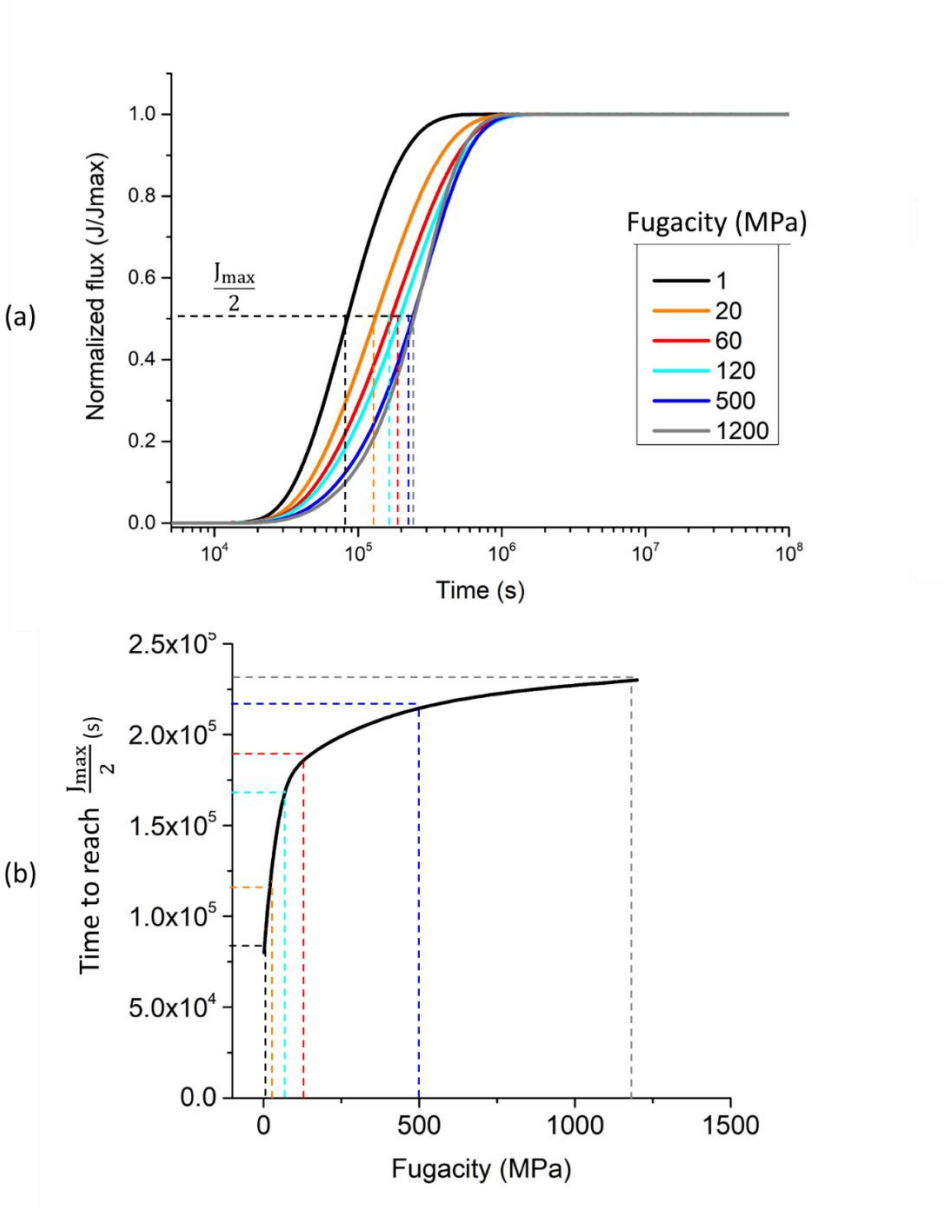

Figure 15: (a) Influence of hydrogen fugacity at the entry side on the permeation behavior ; (b) Evolution of the time needed to reach $J_{max}/2$ as a function of hydrogen fugacity. $K_H = 0.569\ mol/(m^3 \times MPa^{0.5})$; $X_P = 0.04\%$.

3.3. Comparison to the experimental data

In a previous work [12], electrochemical permeation tests were conducted on a cast sample of low-alloy steel (G20MN5) with a porosity fraction of 0.04 ± 0.02% and a forged sample of the same steel in order to highlight the effect of the porosity in hydrogen diffusion and trapping. Hydrogen solubility in the forged material was also determined and it was found equal to 0.569 ± 0.142 mol/(m^3×MPa$^{0.5}$). X-ray tomography measurements have also shown that the average cavity size and inter-cavity distance in the steel investigated were 7.6 µm and 138 µm respectively. The latter implies that there were approximately 15 cavities along the thickness of the permeation specimen (2 mm). In that work, the experimental apparent

diffusion coefficient determined from the 63% time lag method for the cast (porous) and forged materials were 3.7 10^{-12} and 7.8 10^{-12} m²/s respectively. From the permeation curves calculated using the local equilibrium model and presented in Figure 13, an apparent diffusion coefficient was also determined using the 63% time lag method [8] for each porosity fraction investigated. Figure 16 compares these values of D_{app} with those obtained from experiments [12]. The value of D_{app} predicted by the model for a porosity fraction of 0.04 % (2.9 10^{-12} m²/s) is in good agreement with the experimental one (3.7 10^{-12} m²/s). Note that no input parameter of the model was adjusted. The model correctly predicts the decrease of the diffusion coefficient by a factor of 2 to 3 for a porosity fraction of 0.04 ± 0.02%.

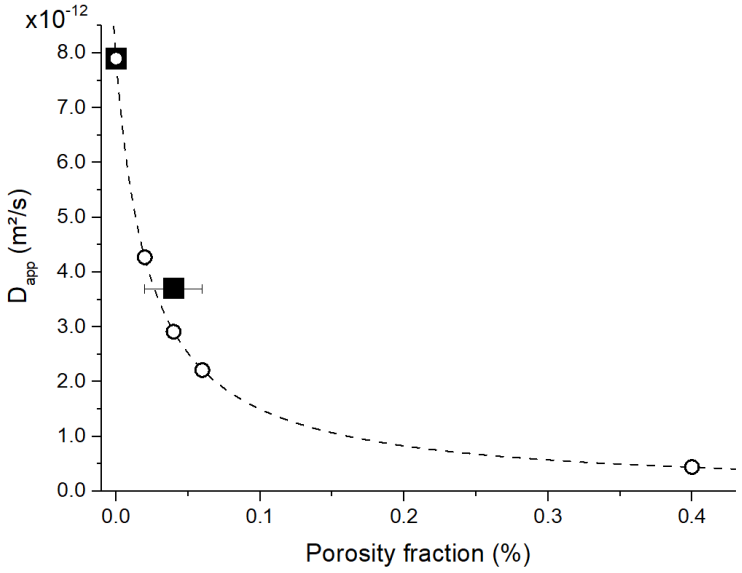

Figure 16: Apparent diffusion coefficient obtained from the local equilibrium model (extracted from the curves of Figure 13 (a)) for different porosity fractions (white circles) compared with the experimental values from [12] (black squares). Note the ± 0.02% error bar on the porosity measurement. The dotted line is only a guide for the eyes.

4. Conclusions

In this study, two numerical models have been proposed in order to simulate hydrogen permeation for a steel containing micro-porosity. These two models take into account the trapping of gaseous hydrogen in cavities. They are based on two different approaches: the first model is based on a non-equilibrium approach, where a reaction flux is considered at the bulk-cavity interface and the second model is based on a local equilibrium approach, between hydrogen dissolved in the bulk and gaseous hydrogen in the cavities. It should be mentioned that the second model is simpler and less time consuming compared to the first model. The numerical models were discussed in detail first and then the results were compared to the

permeation experimental data presented in a previous work. It is important to note that the two models were developed based on a refined EOS, which permits to perform simulations on a wide range of pressure [0, 2000 MPa]. The following main conclusions can be drawn:

- For the non-equilibrium model, an expression of hydrogen flux due to the recombination reaction of atomic hydrogen into molecular hydrogen at the bulk-cavity interface was developed based on a non-equilibrium approach. The flux orientation (inward or outward) is controlled by the hydrogen concentration at the interface and hydrogen fugacity inside the cavity. A choice was made in this study to work in a diffusion-limited regime instead of an interface reaction-limited regime.
- The permeation behavior across a simulation box containing one single cavity was studied in detail. The time evolution of cavity pressure, bulk-cavity interface concentration and permeation flux was found consistent.
- The effect of the number of cavities and their location in the simulation box was studied. For a given porosity fraction, increasing the number of cavities results in larger bulk-cavity interface area and lower cavity volume, which facilitates local equilibrium. When the number of cavities is large enough, the non-equilibrium model gives the same results as the local equilibrium model.
- A parametric study using the local equilibrium model was conducted. The permeation time was found to vary linearly with X_P and $\frac{1}{\mathrm{K_H}}$ where X_P is the porosity fraction in the specimen and K_H is the hydrogen solubility in the bulk material (Sieverts' constant). In addition, it was found that the permeation time increases as the square root of hydrogen fugacity f_{H_2} at the entry side.

- Finally, a comparison between simulations and experiments from a previous study was made and showed a good agreement: the local equilibrium model correctly predicts the decrease of the diffusion coefficient by a factor of 2 to 3 for a porosity fraction of 0.04 ± 0.02%.

Acknowledgments

This study was mainly funded by SafeMetal with the support of ANRT (Association Nationale de la Recherche et de la Technologie). Dr Aurélien Villani is acknowledged for his

help in running the calculations on the computer cluster. Max Boudes is acknowledged for his help in revising the paper.

Data availability statement

The raw and processed data required to reproduce these findings are available from the corresponding author upon request.

References

[1] Gangloff RP. 6.02 - Hydrogen-assisted Cracking. In: Milne I, Ritchie RO, Karihaloo B, editors. Compr. Struct. Integr., Oxford: Pergamon; 2003, p. 31–101. https://doi.org/10.1016/B0-08-043749-4/06134-6.

[2] Oriani RA, Hirth JP, Smialowski M. Hydrogen degradation of ferrous alloys. Park Ridge, N.J., U.S.A.: Noyes Publications; 1985.

[3] Louthan MR, Caskey GR, Donovan JA, Rawl DE. Hydrogen embrittlement of metals. Mater Sci Eng 1972;10:357–68. https://doi.org/10.1016/0025-5416(72)90109-7.

[4] Depover T, Pérez Escobar D, Wallaert E, Zermout Z, Verbeken K. Effect of hydrogen charging on the mechanical properties of advanced high strength steels. Int J Hydrog Energy 2014;39:4647–56. https://doi.org/10.1016/j.ijhydene.2013.12.190.

[5] Srinivasan R, Neeraj T. Hydrogen Embrittlement of Ferritic Steels: Deformation and Failure Mechanisms and Challenges in the Oil and Gas Industry. JOM 2014;66:1377–82. https://doi.org/10.1007/s11837-014-1054-4.

[6] Ohaeri E, Eduok U, Szpunar J. Hydrogen related degradation in pipeline steel: A review. Int J Hydrog Energy 2018;43:14584–617. https://doi.org/10.1016/j.ijhydene.2018.06.064.

[7] Jack TA, Pourazizi R, Ohaeri E, Szpunar J, Zhang J, Qu J. Investigation of the hydrogen induced cracking behaviour of API 5L X65 pipeline steel. Int J Hydrog Energy 2020;45:17671–84. https://doi.org/10.1016/j.ijhydene.2020.04.211.

[8] Martin F, Feaugas X, Oudriss A, Tanguy D, Briottet L, Kittel J. State of Hydrogen in Matter: Fundamental Ad/Absorption, Trapping and Transport Mechanisms. Mech. - Microstruct. - Corros. Coupling, Elsevier; 2019, p. 171–97. https://doi.org/10.1016/B978-1-78548-309-7.50008-9.

[9] Lynch SP. Hydrogen embrittlement (HE) phenomena and mechanisms. Stress Corros. Crack., Elsevier; 2011, p. 90–130. https://doi.org/10.1533/9780857093769.1.90.

[10] Pehlke RD. Formation of Porosity During Solidification of Cast Metals. In: Katz S, Landefeld CF, editors. Foundry Process. Their Chem. Phys., Boston, MA: Springer US; 1988, p. 427–45. https://doi.org/10.1007/978-1-4613-1013-6_17.

[11] Riedler M, Michelic S, Bernhard C. Formation of shrinkage porosity during solidification of steel: Numerical simulation and experimental validation. IOP Conf Ser Mater Sci Eng 2016;143:012035. https://doi.org/10.1088/1757-899X/143/1/012035.

[12] Yaktiti A, Dreano A, Carton JF, Christien F. Hydrogen diffusion and trapping in a steel containing porosities. Corros Sci 2022;199:110208. https://doi.org/10.1016/j.corsci.2022.110208.

[13] Epstein H, Chipman J, Grant NJ. Hydrogen in steelmaking practice. JOM 1957;9:597–608. https://doi.org/10.1007/BF03397917.

[14] Möser M, Schmidt V. FRACTOGRAPHY AND MECHANISM OF HYDROGEN CRACKING - THE FISHEYE CONCEPT. In: Valluri SR, Taplin DMR, Rao PR, Knott JF, Dubey R, editors. Fract. 84, Pergamon; 1984, p. 2459–66. https://doi.org/10.1016/B978-1-4832-8440-8.50254-4.

[15] Yang B, Li L, Cheng L. Numerical Evaluation on Analysis Methods of Trapping Site Density in Steels Based on Hydrogen Permeation Curve. Materials 2020;13:3712. https://doi.org/10.3390/ma13173712.

[16] McNabb, A. ; Foster, P. K. A New Analysis of the Diffusion of Hydrogen in Iron and Ferritic Steels. Trans Met Soc AIME 227 1963 P. 618-627.
[17] Oriani RA. The diffusion and trapping of hydrogen in steel. Acta Metall 1970;18:147–57. https://doi.org/10.1016/0001-6160(70)90078-7.
[18] Kirchheim R. Bulk Diffusion-Controlled Thermal Desorption Spectroscopy with Examples for Hydrogen in Iron. Metall Mater Trans A 2016;47:672–96. https://doi.org/10.1007/s11661-015-3236-2.
[19] Turnbull A, Carroll MW, Ferriss DH. Analysis of hydrogen diffusion and trapping in a 13% chromium martensitic stainless steel. Acta Metall 1989;37:2039–46. https://doi.org/10.1016/0001-6160(89)90089-8.
[20] Leblond JB, Dubois D. A general mathematical description of hydrogen diffusion in steels—I. Derivation of diffusion equations from boltzmann-type transport equations. Acta Metall 1983;31:1459–69. https://doi.org/10.1016/0001-6160(83)90142-6.
[21] Svoboda J, Fischer FD. Modelling for hydrogen diffusion in metals with traps revisited. Acta Mater 2012;60:1211–20. https://doi.org/10.1016/j.actamat.2011.11.025.
[22] Fischer FD, Mori G, Svoboda J. Modelling the influence of trapping on hydrogen permeation in metals. Corros Sci 2013;76:382–9. https://doi.org/10.1016/j.corsci.2013.07.010.
[23] Svoboda J, Mori G, Prethaler A, Fischer FD. Determination of trapping parameters and the chemical diffusion coefficient from hydrogen permeation experiments. Corros Sci 2014;82:93–100. https://doi.org/10.1016/j.corsci.2014.01.002.
[24] Legrand E, Feaugas X, Bouhattate J. Generalized model of desorption kinetics: Characterization of hydrogen trapping in a homogeneous membrane. Int J Hydrog Energy 2014;39:8374–84. https://doi.org/10.1016/j.ijhydene.2014.03.191.
[25] Osman Hoch B, Metsue A, Bouhattate J, Feaugas X. Effects of grain-boundary networks on the macroscopic diffusivity of hydrogen in polycrystalline materials. Comput Mater Sci 2015;97:276–84. https://doi.org/10.1016/j.commatsci.2014.10.048.
[26] Stopher MA, Lang P, Kozeschnik E, Rivera-Diaz-del-Castillo PEJ. Modelling hydrogen migration and trapping in steels. Mater Des 2016;106:205–15. https://doi.org/10.1016/j.matdes.2016.05.051.
[27] Zapffe CA, Sims CE. Hydrogen embrittlement, internal stress and defects in steel. Trans AIME 145 1941:225–61.
[28] Chew B. A Void Model for Hydrogen Diffusion in Steel. Met Sci J 1971;5:195–200. https://doi.org/10.1179/030634571790439531.
[29] Krom AHM, Bakker A. Hydrogen trapping models in steel. Metall Mater Trans B 2000;31:1475–82. https://doi.org/10.1007/s11663-000-0032-0.
[30] Allen-Booth DM, Hewitt J. A mathematical model describing the effects of micro voids upon the diffusion of hydrogen in iron and steel. Acta Metall 1974;22:171–5. https://doi.org/10.1016/0001-6160(74)90007-8.
[31] Fan J, Yan L, Zhou H, Cao E. Variation of cavity hydrogen pressure in the forming process of heavy forging. Int J Adv Manuf Technol 2017;89:1259–67. https://doi.org/10.1007/s00170-016-9185-0.
[32] Quirós C, Mougenot J, Lombardi G, Redolfi M, Brinza O, Charles Y, et al. Blister formation and hydrogen retention in aluminium and beryllium: A modeling and experimental approach. Nucl Mater Energy 2017;12:1178–83. https://doi.org/10.1016/j.nme.2016.12.036.
[33] Ayadi S, Charles Y, Gaspérini M, Caron Lemaire I, Da Silva Botelho T. Effect of loading mode on blistering in iron submitted to plastic prestrain before hydrogen cathodic charging. Int J Hydrog Energy 2017;42:10555–67. https://doi.org/10.1016/j.ijhydene.2017.02.048.
[34] Su H, Toda H, Shimizu K, Uesugi K, Takeuchi A, Watanabe Y. Assessment of hydrogen embrittlement via image-based techniques in Al–Zn–Mg–Cu aluminum alloys. Acta Mater 2019;176:96–108. https://doi.org/10.1016/j.actamat.2019.06.056.
[35] Zibrov M, Schmid K. Reaction–diffusion simulations of hydrogen isotope trapping and release from cavities in tungsten, II: Array of cavities. Nucl Mater Energy 2022;32:101219. https://doi.org/10.1016/j.nme.2022.101219.

[36] Sezgin J-G, Bosch C, Montouchet A, Perrin G, Wolski K. Modelling and simulation of hydrogen redistribution in a heterogeneous alloy during the cooling down to 200 °C. Int J Hydrog Energy 2017;42:19346–58. https://doi.org/10.1016/j.ijhydene.2017.03.095.
[37] Sezgin J-G, Bosch C, Montouchet A, Perrin G, Wolski K. Modelling of hydrogen induced pressurization of internal cavities. Int J Hydrog Energy 2017;42:15403–14. https://doi.org/10.1016/j.ijhydene.2017.04.106.
[38] Fan J, Peng B, Zhao W. Study on hydrogen behaviors around micropores within heavy forging during heating process. Int J Adv Manuf Technol 2021;113:523–33. https://doi.org/10.1007/s00170-021-06660-z.
[39] Zibrov M, Schmid K. Reaction–diffusion simulations of hydrogen isotope trapping and release from cavities in tungsten, I: Single cavity. Nucl Mater Energy 2022;30:101121. https://doi.org/10.1016/j.nme.2022.101121.
[40] Hemond HF, Fechner EJ. Chapter 1 - Basic Concepts. In: Hemond HF, Fechner EJ, editors. Chem. Fate Transp. Environ. Third Ed., Boston: Academic Press; 2015, p. 1–73. https://doi.org/10.1016/B978-0-12-398256-8.00001-3.
[41] Vallero DA. Chapter 4 - Environmental partitioning. In: Vallero DA, editor. Air Pollut. Calc., Elsevier; 2019, p. 73–105. https://doi.org/10.1016/B978-0-12-814934-8.00004-1.
[42] Marchi CS, Somerday BP, Robinson SL. Permeability, solubility and diffusivity of hydrogen isotopes in stainless steels at high gas pressures. Int J Hydrog Energy 2007;32:100–16. https://doi.org/10.1016/j.ijhydene.2006.05.008.
[43] Helmi A. Sieverts' Law. In: Drioli E, Giorno L, editors. Encycl. Membr., Berlin, Heidelberg: Springer; 2015, p. 1–2. https://doi.org/10.1007/978-3-642-40872-4_2192-1.
[44] A. Sieverts. Absorption of Gases by Metals. Z Für Met Vol 21 1929.
[45] Chiranjib Kumar Gupta,. Thermodynamics and Kinetics. Chem. Metall., John Wiley & Sons, Ltd; 2003, p. 225–342. https://doi.org/10.1002/3527602003.ch3.
[46] Somerday BP, Marchi CS. 3 - Hydrogen containment materials. In: Walker G, editor. Solid-State Hydrog. Storage, Woodhead Publishing; 2008, p. 51–81. https://doi.org/10.1533/9781845694944.1.51.
[47] Pekař M. Thermodynamic Driving Forces and Chemical Reaction Fluxes; Reflections on the Steady State 2020. https://doi.org/10.26434/chemrxiv.8217143.v2.
[48] The Transport of Diluted Species Interface n.d. https://doc.comsol.com/5.6/doc/com.comsol.help.battery/battery_ug_chemsptrans.09.002.html (accessed September 6, 2021).
[49] Venezuela J, Tapia-Bastidas C, Zhou Q, Depover T, Verbeken K, Gray E, et al. Determination of the equivalent hydrogen fugacity during electrochemical charging of 3.5NiCrMoV steel. Corros Sci 2018;132:90–106. https://doi.org/10.1016/j.corsci.2017.12.018.